INORGANIC MATERIALS
AND NANOMATERIALS

Synthesis and Chemoresistive Properties of Single-Layer MXene Ti$_2$CT$_x$

E. P. Simonenko^a, *, N. P. Simonenko^a, I. A. Nagornov^a, T. L. Simonenko^a,
Ph. Yu. Gorobtsov^a, A. S. Mokrushin^a, and N. T. Kuznetsov^a

^{a} Kurnakov Institute of General and Inorganic Chemistry, Russian Academy of Sciences, Moscow, 119991 Russia
*e-mail: ep_simonenko@mail.ru

Abstract—As part of the study, we have developed a method for obtaining a single-layer Ti$_2$CT$_x$ MXene by the interaction of Ti$_2$AlC with a mixture of hydrochloric acid and sodium fluoride followed by delamination using a tetramethylammonium hydroxide solution and ultrasonic exposure. The obtained stable aqueous dispersion of Ti$_2$CT$_x$ has been applied by microplotter printing onto a specialized sensor chip, which has been dried at a temperature of 150°C under reduced pressure. The coating has been studied using modern physicochemical methods of analysis. According to the data of X-ray spectral elemental microanalysis, the ratio n(Ti) : n(F + Cl) = 2 : (0.82–0.85), n(F) : n(Cl) ≈ 6 : 4; aluminum impurity does not exceed 1.5–2.0%. Data have been obtained on the local electrophysical properties of the Ti$_2$CT$_x$ coating: on the value of the electron work function from the surface of the material, the distribution of charge carriers, and the capacitance gradient of the "probe tip–sample microregion" capacitor. For the first time, at an operating temperature of 30°C, extremely high chemoresistive responses of the Ti$_2$CT$_x$ receptor layer to the content of 1 and 5% oxygen in nitrogen have been determined, which amounted to 8.6 and >276, respectively.

INTRODUCTION

At present, such a relatively new and wide class of two-dimensional nanomaterials as MXenes is of high scientific and technological interest. As is known, the general formula of these substances is M$_{n+1}$X$_n$T$_x$, in which M is a transition metal, X is carbon or nitrogen, T are surface functional groups (most often F$^-$, OH$^-$, Cl$^-$ or oxygen), and n is 1, 2, and 3 [1–4]. Due to the large variability of the compositions and structure of MXenes, their practically significant properties can be directed to change; however, among the general characteristics, it is necessary to note the high electrical conductivity, the ability to harden when they are introduced into composite materials of various nature due to the large specific surface area [5–9], as well as the possibility of intercalation between layers of different ions [10–12].

Most attention is focused on the use of MXenes in energy generation and storage devices, such as lithium/sodium-ion batteries and supercapacitors [13–19], and fuel cells [20, 21]. However, they are also widely used as a material for transparent conductive coatings, and in optoelectronics [22, 23], photo- and electrocatalytic processes (purification of industrial waters, hydrogen production, CO$_2$ reduction, electro-catalytic reduction of nitrogen with the formation of ammonia, etc.) [24–26].

The unique electrical characteristics inherent in MXenes, the possibility of their directed transformation by changing the chemical composition and structure, and the high specific surface area characteristic of 2D nanomaterials are also in demand in the development of gas sensors [27–33]. Of particular interest is the problem of creating efficient portable devices [27] operating at a minimum (optimally, room) temperature [34]. MXene Ti$_3$C$_2$T$_x$ historically obtained first [34–37] is mainly tested as a receptor material, while for another representative of titanium-containing carbide MXenes, Ti$_2$CT$_x$, information on possible chemoresistive properties is practically absent in the literature. The available studies are mostly computational, while experimental works are sporadic and have been performed for a limited number of gaseous analytes. Thus, using the example of M$_2$CS$_2$ (M = Ti, Zr, Hf) with sulfide surface groups, the prerequisites of this material for increased gas sensitivity with respect to nitrogen oxides NO$_x$ were theoretically shown [38]. In the computational studies [39–41], using the DFT method, conclusions were made about the prospects of single-layer Ti$_2$CO$_2$ MXene as a chemosensor material for gaseous ammonia. In the study [42], based on

the data of quantum chemical calculations for MXene phases with different surface groups (Ti_2C, Ti_2CF_2, and $Ti_2C(OH)_2$), a high potential is predicted for the detection of phosgene, especially for the latter hydroxo-substituted compound.

In [43], for a multilayer Ti_2CT_x exhibiting p-type semiconductor properties, the possibility of detecting at room temperature and photoexcitation with visible light such an explosive analyte of practical importance as methane was experimentally shown: the response to 1% CH_4 was 142%, and the response to 1000 ppm was 68% with moderate response and recovery times (38 and 47 s, respectively).

The purpose of this work is the synthesis and comprehensive study of the gas sensitive properties of MXene Ti_2CT_x when using it as a material for a chemoresistive gas sensor.

EXPERIMENTAL

For the synthesis of MXene Ti_2CT_x, we used powder MAX phase Ti_2AlC, the synthesis procedure of which was described in detail [44]. The content of the main substance was 86%; 1.6% TiC was found as crystalline impurities, as well as intermetallic compounds Ti_3Al (3.8%) and TiAl (8.6%). Ti_2AlC was synthesized based on metal and graphite powders in the ratio $n(Ti) : n(Al) : n(C) = 2 : 1.2 : 0.8$ at a temperature of 1000°C in air in a protective KBr melt [45, 46].

Preliminary experiments on the removal of an aluminum layer from the Ti_2AlC composition by etching in an HF solution described in [45, 47–50] showed that these approaches are not efficient enough to obtain Ti_2CT_x MXene. In this regard, the efficiency of selective aluminum etching was studied using hydrogen fluoride released in situ during the interaction of a hydrochloric acid solution and an alkali metal fluoride (Fig. 1a). In most sources, it is proposed to use LiF for these purposes [43, 51, 52]; this system is quite effective for most MAX phases, for example, Ti_3AlC_2. However, in the present experiment, in order to avoid contamination of the product by the poorly soluble LiF in water, we proposed to use NaF (special purity grade 9-2, Reakhim, Russia), which was previously used for less reactive MAX phases of the M_2AlC composition, for example, in order to obtain MXene V_2CT_x [53–57], which is synthesized under more stringent conditions. To obtain Ti_2CT_x, a weighed portion of 1 g of sodium fluoride was dissolved in 20 mL of a 6 M hydrochloric acid solution (>99%, Sigma Tech, Russia). The Ti_2AlC MAX phase (1 g) synthesized earlier was added in parts to the obtained solution. After that, the reaction system was placed in a water bath and kept under stirring at a temperature of 40 ± 5°C for 24 h. The resulting dark suspension was centrifuged at 3500 rpm for 60 min, the swamp-green supernatant was decanted, and the solid reaction product was repeatedly washed with distilled water separating the solid phase by centrifugation until pH ~5–6 was reached.

Delamination of the resulting multilayer MXene was performed with a solution of tetramethylammonium hydroxide $(CH_3)_4N(OH)$ (25%, aqueous solution, Technic, France) under ultrasonic action [58–60] (Fig. 1a). Then, the residual solid phase was separated by centrifugation followed by washing with deoxygenated water to pH ~6–7 in the resulting dispersion of MXene.

To create MXene coatings, a sample of an aqueous dispersion was used, which, after synthesis and delamination, was stored in the dark and at a low temperature for 15 days. Ti_2CT_x MXene layers were deposited on the surface of a glass plate and a specialized chip by microplotter printing using a three-coordinate positioning system and a glass capillary with an outlet diameter of 150 μm. The formation of a coating with lateral dimensions of 5×3 mm on the front surface of the chip, which is a plate of Al_2O_3 ($R_a = 100$ nm) with deposited platinum interdigital electrodes and a microheater on the reverse side, was carried out according to a given program at a rate of 100 mm/min. The coatings were dried at a temperature of 150°C under reduced pressure for 30 min.

X-ray diffraction patterns of the initial Ti_2AlC MAX-phase sample, as well as layers of Ti_2CT_x MXene on glass and a specialized sensor, were recorded on a Bruker D8 Advance X-ray diffractometer (CuK_α radiation, resolution 0.02° with signal accumulation at a point for 0.3 s). X-ray powder diffraction was performed using MATCH!—Phase Identification from Powder Diffraction, Version 3.8.0.137 (Crystal Impact, Germany), Crystallography Open Database (COD), supplemented with data for the Ti_2AlC hexagonal phase.

The microstructure of the resulting Ti_2CT_x MXene was studied using transmission electron microscopy (TEM, Jeol JEM-1011 instrument with Orius SC1000W digital camera) and scanning electron microscopy (SEM, NVision 40 three-beam workstation, Carl Zeiss). The elemental composition of the samples was assessed in areas of 45×60 μm using an EDX Oxford Instruments X-MAX 80 X-ray elemental microanalysis attachment.

The resulting films of Ti_2CT_x MXene were studied by atomic force microscopy (AFM) on a Solver Pro-M scanning probe microscope (NT-MDT) using ETALON HA-HR probes with a conductive coating based on W_2C (resonant frequency ~367 kHz, rounding radius <35 nm). The measurements were performed using both AFM with recording of the material surface topography and Kelvin probe force microscopy.

The gas sensitive properties were measured on a special precision setup using a model sensor substrate
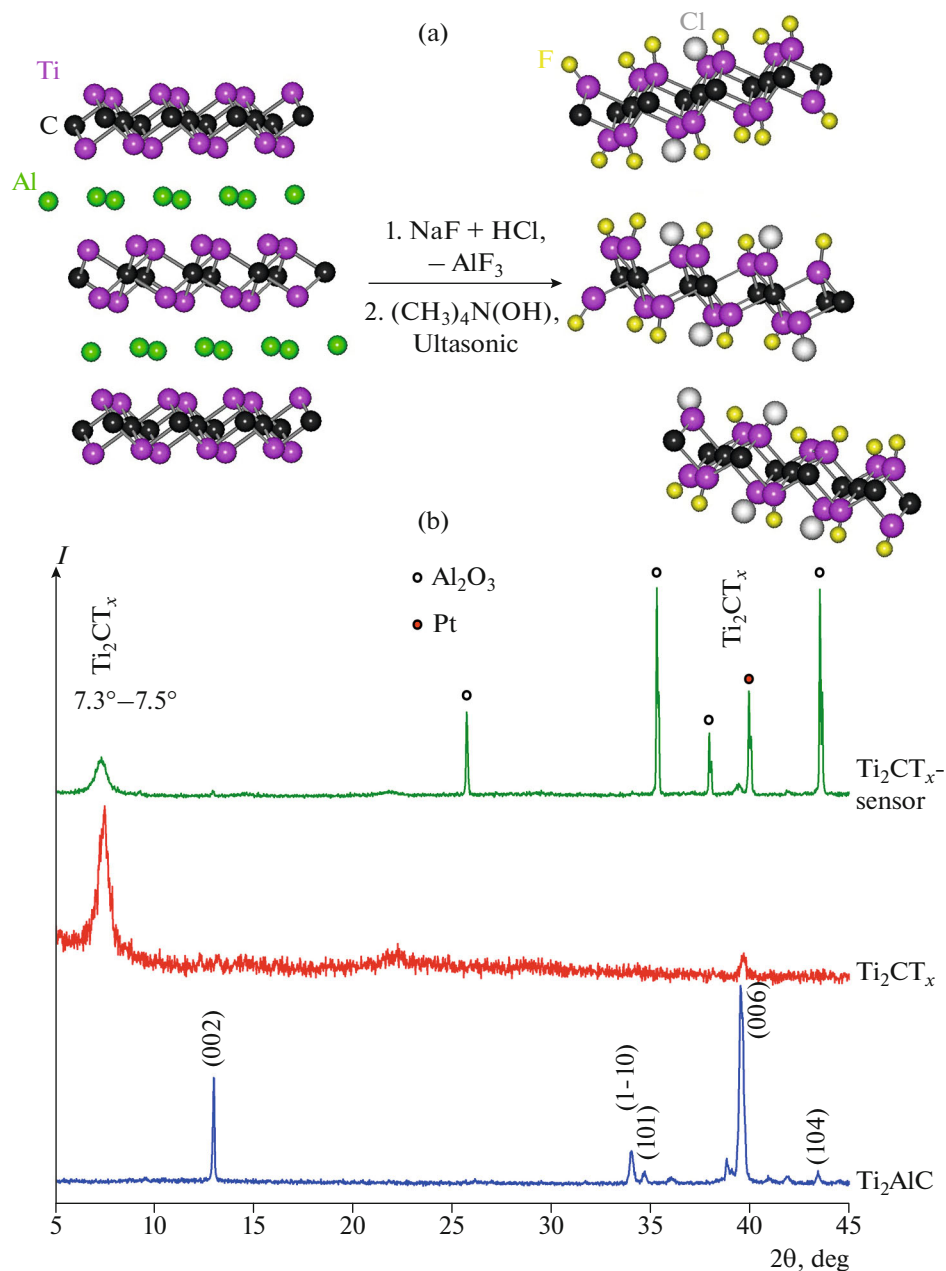
Fig. 1. (a) Scheme of the production of Ti_2CT_x MXene and (b) X-ray diffraction patterns of the initial Ti_2AlC MAX phase and layers of the resulting product Ti_2CT_x on glass and sensor substrates.

[61−65]. The gaseous medium was created in a quartz cell using two Bronkhorst gas flow controllers with a maximum throughput of 100 and 200 mL/min. The temperature of the sensor element was controlled using a platinum microheater on the reverse side of the sensor. The resulting film was studied for sensitivity to various analyte gases: H_2, CO, NH_3, NO_2, benzene (C_6H_6), acetone (C_3H_6O), ethanol (C_2H_5OH), and O_2. The resistance of the receptor materials was measured using a Fluke 8846A digital multimeter (6.5 Digit Precision Multimeter) with an upper limit of 1 GΩ. Nitrogen (99.9995%) was used as a reference gas for oxygen detection, and synthetic air was used for other analyte gases.

Responses (%) to H_2, CO, NH_3, NO_2, C_6H_6, C_3H_6O, and C_2H_5OH were calculated using the formula:

$$S = |R_g - R_{air}| \times 100 / R_{air}, \quad (1)$$

where R_g is the resistance at a given analyte gas concentration; R_{air} is the air resistance.

The responses (relative units) to O_2 were calculated using the formula:

$$S = R_{O_2}/R, \qquad (2)$$

where R_{O_2} is the resistance at a given oxygen concentration; R is the resistance in nitrogen atmosphere.

RESULTS AND DISCUSSION

X-ray powder diffraction studies showed (Fig. 1b) that, after exposure to a mixture of hydrochloric acid and sodium fluoride, the coatings of the Ti_2CT_x product contain no impurities of the initial MAX phase, as well as usually difficult-to-separate aluminum fluorides and highly dispersed titanium carbide. The impurities of intermetallic compounds Ti_3Al and $TiAl$ present in the initial Ti_2AlC were also not found. The characteristic shift of reflection (002) towards smaller angles ($2\theta = 7.3°-7.5°$) indicates a significant increase in the interlayer distance in the Ti_2CT_x coatings both on glass and on the Al_2O_3 ceramic substrate (Fig. 1b, red and green curves) as a result of the removal of the interlayer of aluminum atoms in the composition of the Ti_2AlC MAX phase, its replacement by $-F$, $-Cl$, and $-OH$ surface groups, and delamination.

According to TEM data (Fig. 2), the resulting Ti_2CT_x is single layer, which is typical of etching products with HCl + MF systems, where $M = Li^+$, Na^+, K^+, NH_4^+, followed by their delamination with quaternary amine hydroxides. In this case, plates with a length of ~200−500 nm (up to 1 μm) are formed, in which defects occur. Agglomerates of fine elongated particles (diameter 3−5 nm, length 6−20 nm) are formed at the edges of the MXene plates: probably, as the dispersion is stored, even in the absence of light and at low temperatures (~5−10°C), they are subjected to degradation by dissolved in water with oxygen, as stated in the literature [66]. This process is also expressed in the loss of aggregative stability of the dispersion and the formation of curdy precipitate during storage, which is practically not amenable to redispersion in water. Nevertheless, even after 45 days of storage at a temperature of 4−6°C in the dark, some of the Ti_2CT_x MXene layers still remain in the samples (Fig. 3).

To study the elemental composition and microstructure of the Ti_2CT_x MXene coating, an aqueous suspension was applied to the surface of a specialized ceramic sensor followed by drying in vacuum at a temperature of 150°C. According to the SEM data (Fig. 4), during the formation of the coating, individual layers of MXene are oriented along the plane of the substrate and form a continuous film with a folded relief. Globular particles ~50−100 nm in size observed can be attributed to impurities of both AlF_3 and the initial MAX phase.

Using EDX analysis, it was found that the content of residual aluminum does not exceed 1.5−2.0%. In this case, the number of halide surface groups varies depending on the studied area in accordance with the ratio $n(Ti) : n(F + Cl) = 2 : (0.82-0.85)$, while the ratio of the amounts of F^- and Cl^- is approximately 6 : 4.

For the resulting coatings of the Ti_2CT_x MXene, the AFM method recorded the topography of the surface of the material (Fig. 5), and using the Kelvin probe force microscopy method, data were obtained on local electrophysical properties, such as the work function of an electron from the surface of materials, the distribution of charge carriers, and the capacitance gradient of the "probe tip−microregion sample."

AFM studies are in good agreement with the data obtained using SEM and TEM. From the topographic image shown in Fig. 5a, it is clear that there are many elongated formations on the surface of the material, rising ~200 nm above the surrounding surface. Layers no thicker than 40−50 nm are clearly distinguished in these formations. Most likely, these are vertically arranged folds of MXene sheets. Between these folds, there are fairly even sections of the horizontal surface covered with elongated nanoparticles up to 80 nm long and up to ~30 nm wide, which are clearly visible in the image obtained by scanning such a surface area in the phase contrast mode (Fig. 5b). Similar particles are present in the TEM micrographs and most likely belong to the aggregates of Ti_2CT_x degradation products.

In addition to topography, maps of the distribution of the surface potential (the Kelvin probe force microscopy mode, Fig. 5c) and the capacitance gradient "probe tip−sample microregion" (SEM mode, Fig. 5d) were obtained as a result of AFM. When considering the results of Kelvin probe force microscopy, we can conclude that the surface potential is not completely uniformly distributed over the area of the sample and there are regions that differ markedly in its value. Folds of MXene sheets are characterized by the highest contact potential difference (the lightest areas in Fig. 5c), while the surface areas covered with nanoparticles differ from each other: the contact potential difference in such a surface area located in the center varies in the range of 570−580 mV, while in the lower right corner, regions with a difference of 549−555 mV are distinguished. Most likely, this difference can be explained by the different oxygen content in the Ti_2CT_x degradation products in different parts of the sample. The SEM results show that the gradient takes a smaller value in the folds of the MXene and the largest one in the depressions and at some boundaries between the folds of the sheets and the areas covered with degradation products, which indicates a shift of charge carriers to these areas. Dark lines are visible, especially in the lower right part of Fig. 5d, on which the gradient also decreases. Some of these lines are also present at some boundaries between the folds of MXene sheets and the surface covered with Ti_2CT_x decomposition products. It is possible that these lines
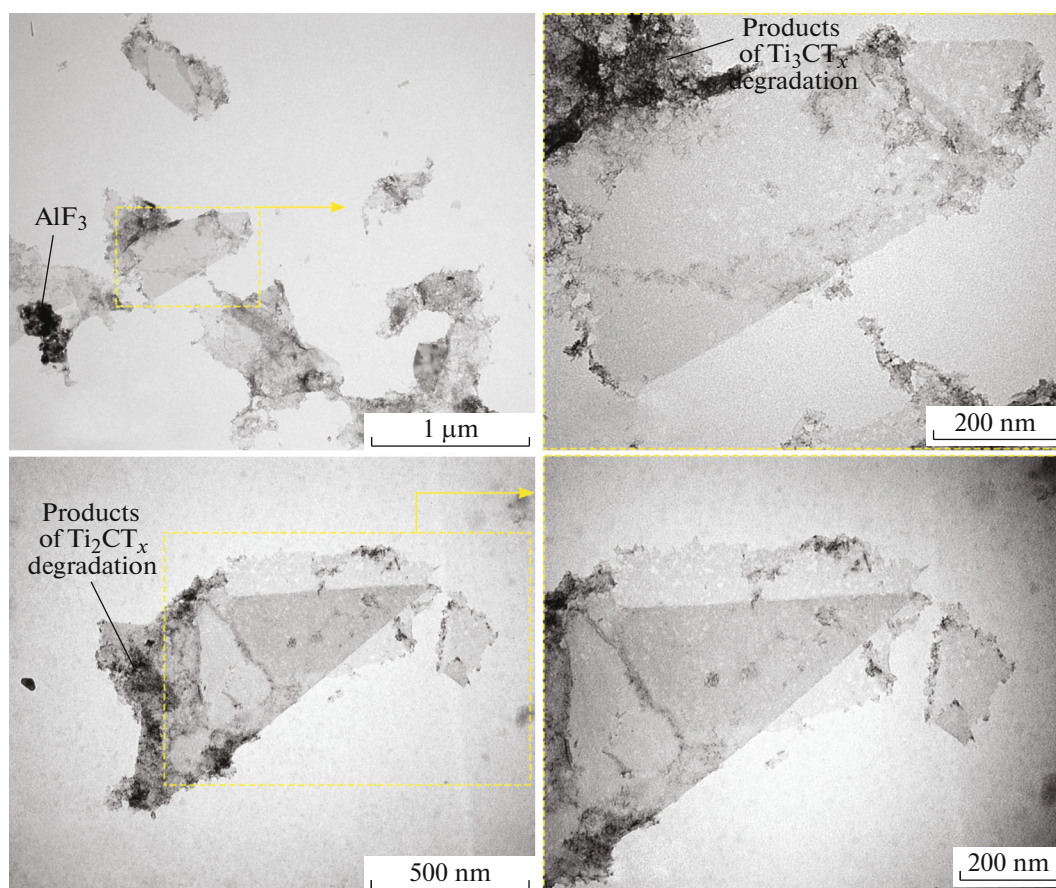
Fig. 2. Microstructure (according to TEM data) of Ti_2CT_x particles, storage of an aqueous dispersion at a temperature of $5-10°C$ in the dark for 15 days.

show the localization of the AlF_3 impurity, which differs significantly in electrical conductivity, or mark the boundaries between different phases; however, in general, its nature is not completely clear. The lower right part of Fig. 5d also shows a region with a strongly reduced gradient value in almost the same area as in Fig. 5c, where a reduced contact potential difference is observed, which indirectly confirms the assumption about the difference in the composition of the products of MXene degradation in different parts of the sample.

The work function for the sample was calculated based on the data obtained using Kelvin probe force microscopy. The obtained value of 4.32 eV is lower than that observed for Ti_2CT_x with a surface modified with fluoride or fluoride and hydroxyl functional groups, namely, 4.98−5.00 eV [67, 68]. A higher work function should also be observed in the case of Ti_2C without any functional groups, about 4.5 eV [68]. Unfortunately, in [67], where the work function of MXene $Ti_2C(OH)_xF_y$ was experimentally determined using Kelvin probe force microscopy, it was not indicated whether the work function was determined (in air or in vacuum), which is very important, since often

a layer of moisture formed on the surface material reduces the measured value of the work function. Thus, it can be assumed that, in this case, the reduced work function can be explained by the presence of a surface layer of air moisture or an increased amount of hydroxyl groups on the surface of the sample, as well as the presence of AlF_3 impurities and products of decomposition of the MXene.

The screening of the chemoresistive properties of the resulting Ti_2CT_x film was performed on the following series of gaseous analytes: 100 ppm CO, 100 ppm NH_3, 500 ppm H_2, 100 ppm NO_2 and 100 ppm C_6H_6, 100 ppm C_3H_6O, and 100 ppm C_2H_5OH, among which ammonia and nitrogen dioxide can be noted, for which such sensitivity was predicted in theoretical works ([38, 69] for NO_x and [39−41] for NH_3). It has been preliminarily determined that the electrical conductivity of the coating in an atmosphere of dry air with an increase in temperature from 30 to 50°C sharply increases from 9.3 to 450 MΩ, which indicates the metallic nature of the conductivity of the sample. Figure 6 shows the responses to these gases measured at detection temperatures of 30 and 50°C. It can be seen that at an operating temperature of 30°C, the film
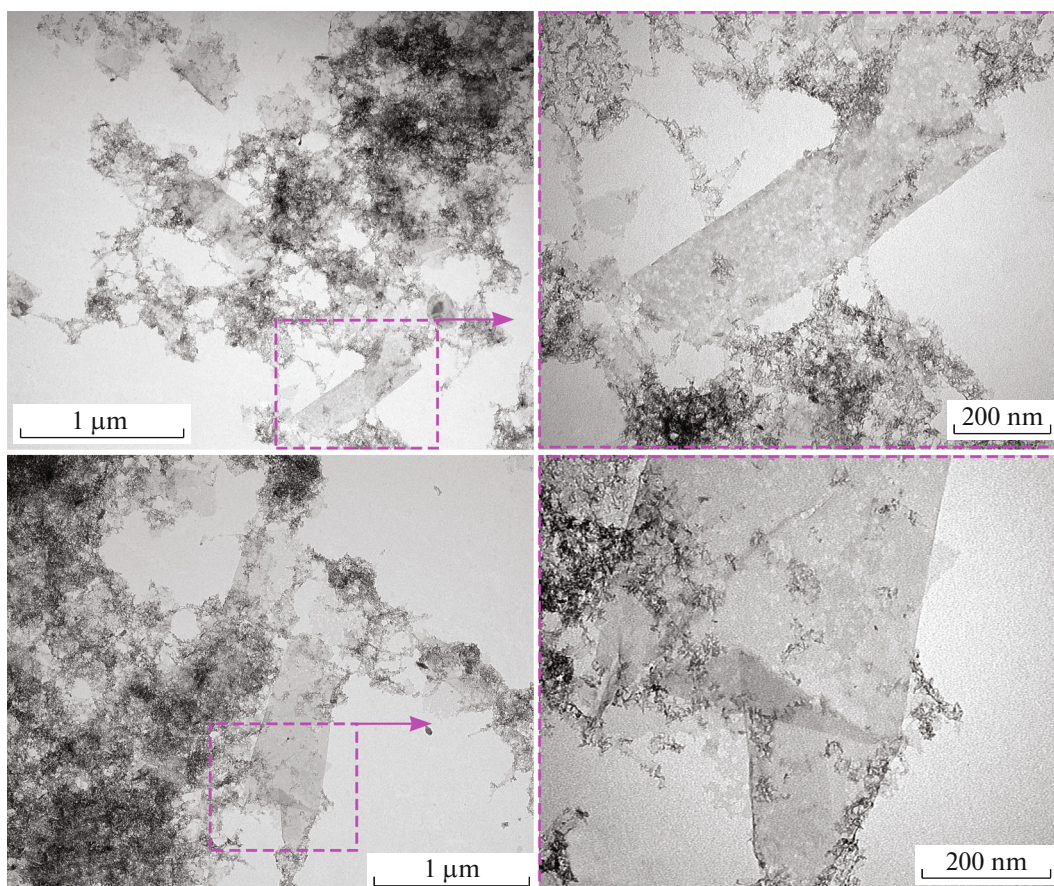
Fig. 3. Microstructure (according to TEM data) of Ti_2CT_x particles, storage of an aqueous dispersion at a temperature of $5-10°C$ in the dark for 45 days.
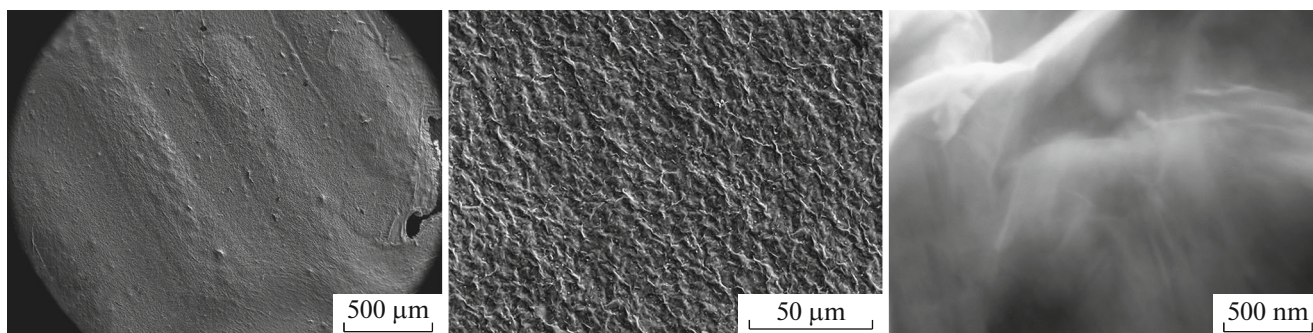

Fig. 4. Surface microstructure of a section of the sensor substrate with interdigital electrodes coated with the Ti_2CT_x receptor layer.

is not sensitive to all gases except NO_2. The response to NO_2 was about 6%, and the baseline resistance increased irreversibly after the cessation of gas puffing, which may indicate irreversible processes on the surface of the receptor material and/or high adsorption energy.

With an increase in the operating temperature to 50°C (Fig. 6b), a significant increase in the resistance

of the Ti_2CT_x coating is observed, as noted above, and a significant increase in noise during signal pickup is detected. The response to H_2, CO, NO_2, C_6H_6, C_3H_6O, and C_2H_5OH is commensurate with the noise and does not exceed 5−6%. The highest response (13%) at 50°C is observed for NH_3. Moreover, in this case, there is no rapid return of the resistance value when pure air is admitted, which may be due to the
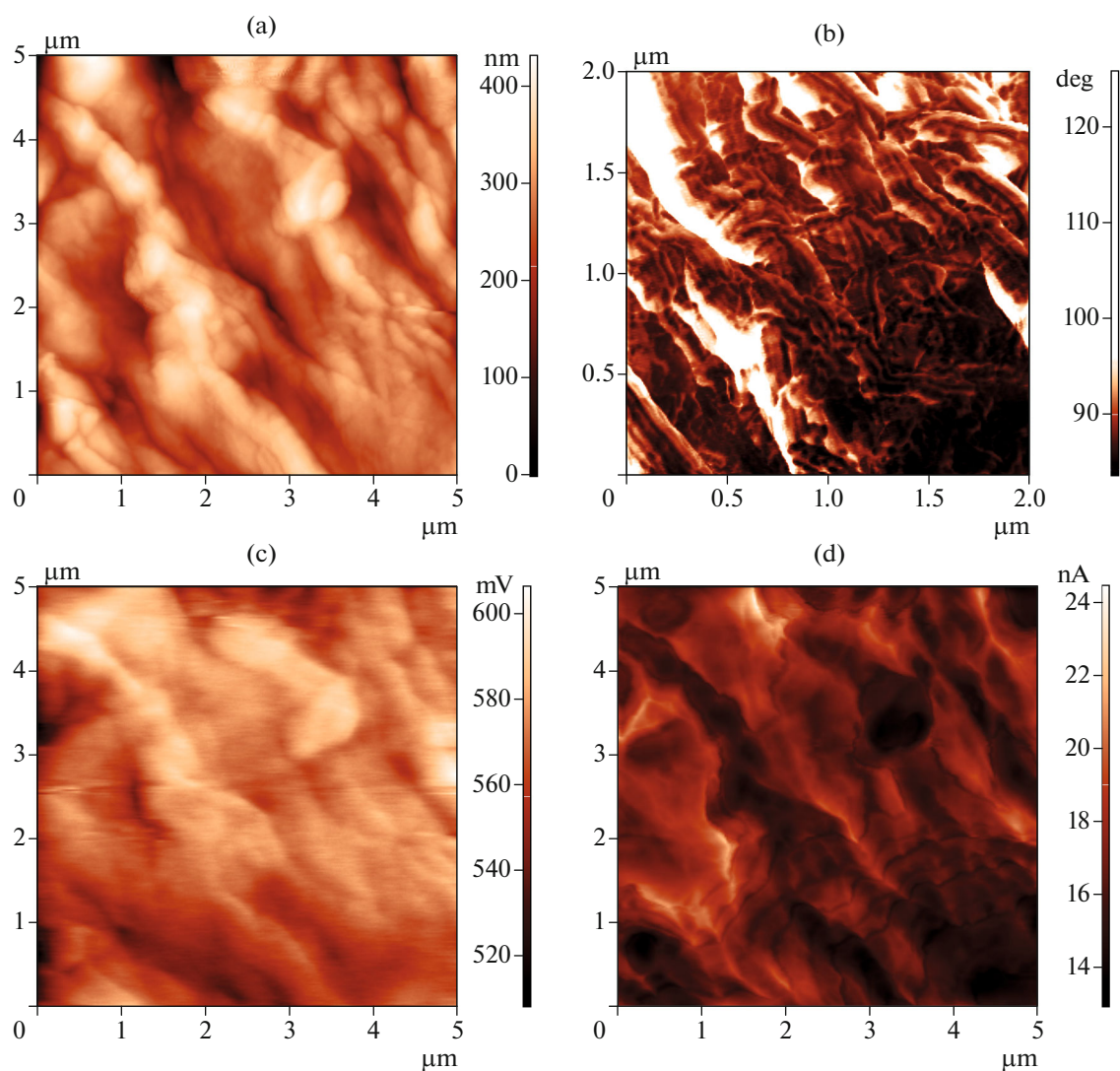
Fig. 5. Results of AFM of the Ti$_2$CT$_x$ film: (a) topography, (b) phase contrast, (c) surface potential map, and (d) capacitance gradient map "probe tip–sample microregion."

strong adsorption interactions between MXene, especially containing hydroxide surface groups, and the ammonia molecule noted in theoretical works [39–41].

The most interesting were the results of detection of oxygen by the obtained receptor material in comparison with individual nitrogen. Figure 7 shows the kinetic curves of the change in the resistance of the coating during the puffing of the gas mixture and the corresponding responses to 1 and 5% O$_2$ (in rel. units, calculated in accordance with Eq. (2)). When 1 and 5% O$_2$ are injected, a significant increase in resistance is observed, the response to 1% O$_2$ is 8.6, and the response to 5% O$_2$ it is significantly higher than 276. It was not possible to accurately determine the last value, since when 5% O$_2$ is injected, the resistance increases above 1 GΩ. It should be noted that after the oxygen supply is stopped, the resistance returns to its original

values, which indicates the reproducibility of the signals. With a further increase in the operating temperature in a nitrogen atmosphere, a significant increase in resistance is observed, which prevents the determination of the response to the oxidizing gas even at a temperature of 50°C.

CONCLUSIONS

Here, a method was developed for obtaining a single-layer Ti$_2$CT$_x$ MXene as a result of the interaction of Ti$_2$AlC with a mixture of hydrochloric acid and sodium fluoride followed by delamination in a tetramethylammonium hydroxide solution and under ultrasonic exposure. The shift of reflection (002) towards smaller angles (to $2\theta = 7.3°-7.5°$) observed in the X-ray diffraction patterns of coatings deposited from the resulting aqueous dispersions on glass and a
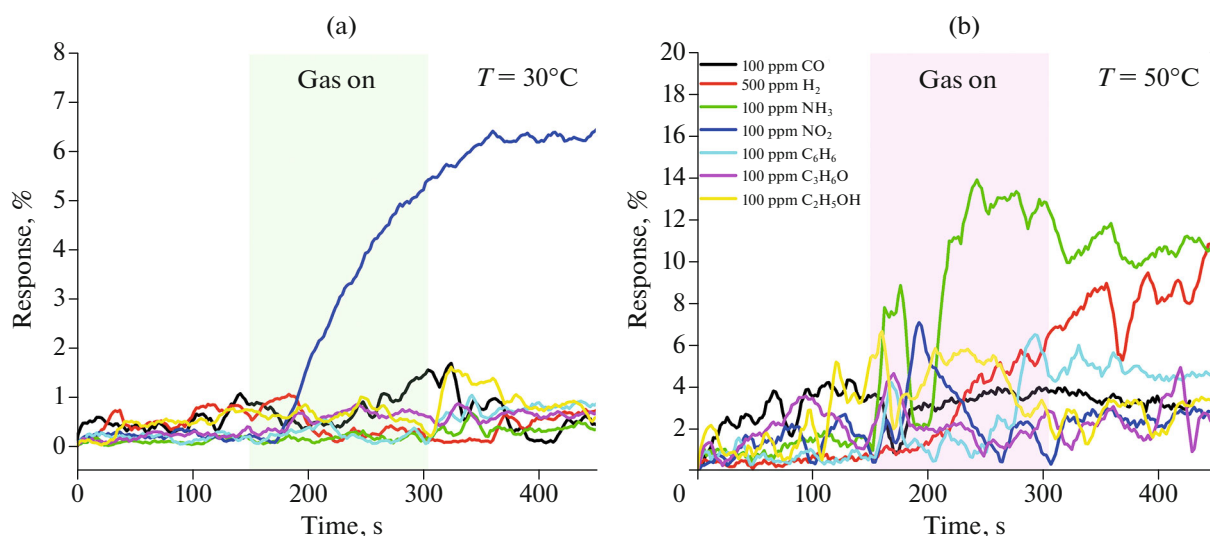
Fig. 6. Screening results for the gas sensitivity of the Ti_2CT_x coating to various analytes at (a) 30 and (b) 50°C.

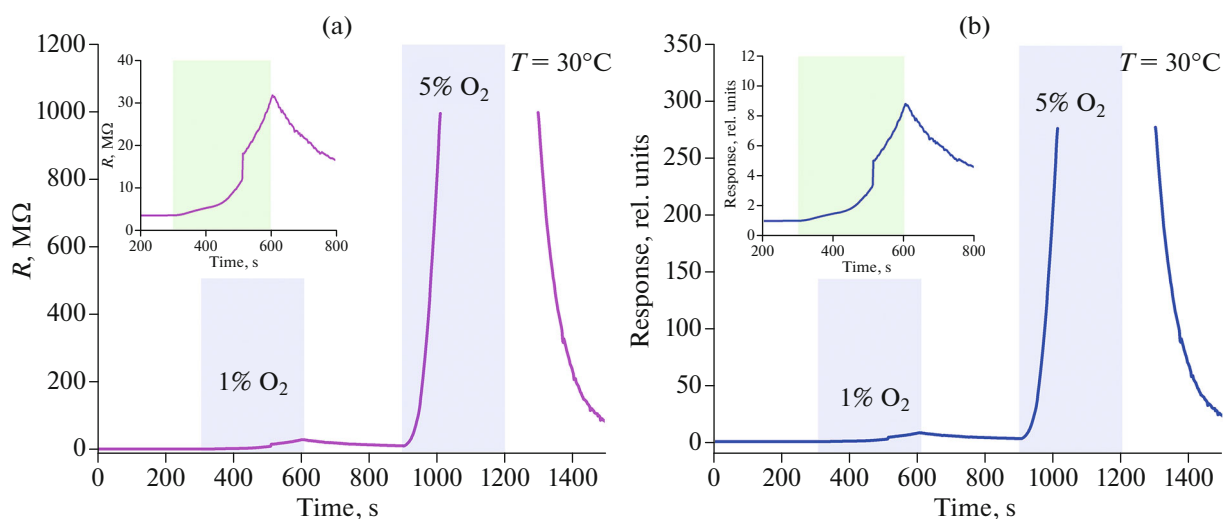**Fig. 7.** (a) Change in the resistance of the receptor material of the Ti_2CT_x coating when puffing gas mixture with 1 and 5% O_2 and (b) the corresponding responses in rel. units R_{O_2}/R; operating temperature 30°C.

specialized sensor ceramic substrate indicates a significant increase in interlayer distance between Ti_2CT_x layers after removal of aluminum from the interlayer space and its replacement by −F, −Cl, and −OH surface groups. The ratio $n(F) : n(Cl)$ determined using X-ray elemental microanalysis of the coating on the sensor is approximately 6 : 4, and $n(Ti) : n(F + Cl) = 2 : (0.82–0.85)$. The content of residual aluminum does not exceed 1.5–2.0%. It has been shown by TEM that for the resulting Ti_2CT_x MXene, the size of the wafers is ~200–500 nm (up to 1 μm). During storage, even at a low temperature and in the dark, degradation of this MXene occurs: agglomerates of oblong nanoparticles (diameter 3–5 nm, length 6–20 nm) are

formed at the edges of the layers. However, even during long-term (up to 45 days) storage, the amount of MXene particles remains significant.

For the Ti_2CT_x MXene coatings deposited on the sensor chip, data were obtained on local electrophysical properties: on the work function of an electron from the material surface, the distribution of charge carriers, and the capacitance gradient of the "probe tip−sample microregion."

Screening of the chemoresistive properties of the resulting Ti_2CT_x film showed an increased gas sensitivity to NO_2 (at an operating temperature of 30°C) and NH_3 (at 50°C) in air with an irreversible increase in resistance or with too long sensor recovery time.

A study of sensitivity to oxygen (1 and 5% O_2 in nitrogen) resulted in extremely high responses at a detection temperature of 30°C close to room temperature. When 1% O_2 was puffed, the response was 8.6 (R_{O_2}/R); the response to 5% O_2 significantly exceeded 276. The mechanism of oxygen detection by chemoresistive gas sensors has not been reliably studied at present and requires additional experiments. The complex shape of the 1% O_2 sorption curve obtained in this work indicates the possibility of multistage surface interactions, the nature of which can be significantly affected by the chemical composition of Ti_2CT_x surface substituents (the presence and quantitative ratio of F^-, Cl^-, and OH^- groups, which is determined by the method of substance synthesis and the mode of application of receptor layers), as well as the degree and products of degradation of the MXene planes.

FUNDING

CONFLICT OF INTEREST

The authors declare that they have no conflicts of interest.

OPEN ACCESS

REFERENCES

1. B. Anasori, M. R. Lukatskaya, and Y. Gogotsi, Nat. Rev. Mater. **2**, 16098 (2017).
https://doi.org/10.1038/natrevmats.2016.98
2. M. Naguib, V. N. Mochalin, M. W. Barsoum, et al., Adv. Mater. **26**, 992 (2014).
https://doi.org/10.1002/adma.201304138
3. M. Naguib, O. Mashtalir, J. Carle, et al., ACS Nano **6**, 1322 (2012).
https://doi.org/10.1021/nn204153h
4. B. Anasori, Y. Xie, M. Beidaghi, et al., ACS Nano **9**, 9507 (2019).
https://doi.org/10.1021/acsnano.5b03591
5. W. Li, B. Zhao, J. Bai, et al., Appl. Surf. Sci. **599**, 153910 (2022).
https://doi.org/10.1016/j.apsusc.2022.153910
6. M. Malaki and R. S. Varma, Adv. Mater. **32**, 2003154 (2020).
https://doi.org/10.1002/adma.202003154
7. Z.-H. Zeng, N. Wu, J.-J. Wei, et al., Nano-Micro Lett. **14**, 59 (2022).
https://doi.org/10.1007/s40820-022-00800-0
8. W. Chen, P. Liu, Y. Liu, et al., Chem. Eng. J. **446**, 137239 (2022).
https://doi.org/10.1016/j.cej.2022.137239
9. S. A. Jasim, J. M. Hadi, M. J. C. Opulencia, et al., J. Alloys Compd. **917**, 165404 (2022).
https://doi.org/10.1016/j.jallcom.2022.165404
10. M. R. Lukatskaya, O. Mashtalir, C. E. Ren, et al., Science **341**, 1502 (2013).
https://doi.org/10.1126/science.1241488
11. Z. Wang, Y. Wang, Q. Gu, et al., Particuology **72**, 10 (2023).
https://doi.org/10.1016/j.partic.2022.02.006
12. X. Zhou, J. Wen, X. Ma, et al., J. Colloid Interface Sci. **624**, 505 (2022).
https://doi.org/10.1016/j.jcis.2022.05.166
13. M. K. Aslam and M. Xu, Nanoscale **12**, 15993 (2020).
https://doi.org/10.1039/D0NR04111D
14. K. S. Kumar, N. Choudhary, Y. Jung, et al., ACS Energy Lett. **3**, 482 (2018).
https://doi.org/10.1021/acsenergylett.7b01169
15. NgV. M. Hong, H. Huang, K. Zhou, et al., J. Mater. Chem. A **5**, 3039 (2017).
https://doi.org/10.1039/C6TA06772G
16. M. Naguib, J. Come, B. Dyatkin, et al., Electrochem. Commun. **16**, 61 (2012).
https://doi.org/10.1016/j.elecom.2012.01.002
17. M. R. Lukatskaya, S. Kota, Z. Lin, et al., Nat. Energy **2**, 17105 (2017).
https://doi.org/10.1038/nenergy.2017.105
18. J. Pang, R. G. Mendes, A. Bachmatiuk, et al., Chem. Soc. Rev. **48**, 72 (2019).
https://doi.org/10.1039/C8CS00324F
19. B. Bharti, Y. Kumar, M. Gupta, et al., ECS Trans. **107**, 1751 (2022).
https://doi.org/10.1149/10701.1751ecst
20. K. Khan, A. K. Tareen, M. Aslam, et al., Nanoscale **11**, 21622 (2019).
https://doi.org/10.1039/C9NR05919A
21. Y. Zhong, X. Xia, F. Shi, et al., Adv. Sci. **3**, 1500286 (2016).
https://doi.org/10.1002/advs.201500286
22. C. Shang, Y. Zhang, G. Wang, et al., J. Alloys Compd. **918**, 165580 (2022).
https://doi.org/10.1016/j.jallcom.2022.165580
23. V. Pacheco-Pena, T. Hallam, and N. Healy, Light Sci. Appl. **11**, 22 (2022).
https://doi.org/10.1038/s41377-022-00710-1
24. X. Xie and N. Zhang, Adv. Funct. Mater. **30**, 2002528 (2020).
https://doi.org/10.1002/adfm.202002528
25. K. Li, S. Zhang, Y. Li, et al., Chinese J. Catal. **42**, 3 (2021).
https://doi.org/10.1016/S1872-2067(20)63630-0
26. F. Naseem, P. Lu, J. Zeng, et al., ACS Nano **14**, 7734 (2020).
https://doi.org/10.1021/acsnano.0c02731
27. M. Xin, J. Li, Z. Ma, et al., Front. Chem. **8** (2020).
https://doi.org/10.3389/fchem.2020.00297

28. X. Liu, H. Zhang, Y. Song, et al., Sensors Actuators, B: Chem. **367**, 132025 (2022). https://doi.org/10.1016/j.snb.2022.132025

29. B. Wang, Y. Gu, L. Chen, et al., Nanotechnology **33**, 252001 (2022). https://doi.org/10.1088/1361-6528/ac5df5

30. S. Nahirniak and B. Saruhan, Sensors **22**, 972 (2022). https://doi.org/10.3390/s22030972

31. Q. Li, Y. Li, and W. Zeng, Chemosensors **9**, 225 (2021). https://doi.org/10.3390/chemosensors9080225

32. R. Bhardwaj and A. Hazra, J. Mater. Chem. C **9**, 15735 (2021). https://doi.org/10.1039/D1TC04085E

33. AghaeiS. Mehdi, A. Aasi, and B. Panchapakesan, ACS Omega **6**, 2450 (2021). https://doi.org/10.1021/acsomega.0c05766

34. E. Lee, A. VahidMohammadi, B. C. Prorok, et al., ACS Appl. Mater. Interfaces **9**, 37184 (2017). https://doi.org/10.1021/acsami.7b11055

35. M. Naguib, M. Kurtoglu, V. Presser, et al., Adv. Mater. **23**, 4248 (2011). https://doi.org/10.1002/adma.201102306

36. S. J. Kim, H.-J. Koh, C. E. Ren, et al., ACS Nano **12**, 986 (2018). https://doi.org/10.1021/acsnano.7b07460

37. Y. Pei, X. Zhang, Z. Hui, et al., ACS Nano **15**, 3996 (2021). https://doi.org/10.1021/acsnano.1c00248

38. C. Hu, X. Yu, Y. Li, et al., Appl. Surf. Sci. **592**, 153296 (2022). https://doi.org/10.1016/j.apsusc.2022.153296

39. X.-H. Li, H.-L. Cui, R.-Z. Zhang, et al., Vacuum **179**, 109574 (2020). https://doi.org/10.1016/j.vacuum.2020.109574

40. L. Xiao-Hong, L. Shan-Shan, Y. Yong-Liang, et al., Appl. Surf. Sci. **504**, 144325 (2020). https://doi.org/10.1016/j.apsusc.2019.144325

41. X. Yu, Y. Li, J. Cheng, et al., ACS Appl. Mater. Interfaces **7**, 13707 (2015). https://doi.org/10.1021/acsami.5b03737

42. S. Thomas and M. A. Zaeem, Adv. Theor. Sim. **4**, 2000250 (2021). https://doi.org/10.1002/adts.202000250

43. J. Wang, R. Xu, Y. Xia, et al., Ceram. Int. **47**, 34437 (2021). https://doi.org/10.1016/j.ceramint.2021.08.357

44. E. P. Simonenko, N. P. Simonenko, I. A. Nagornov, et al., Russ. J. Inorg. Chem. **67**, 705 (2022). https://doi.org/10.1134/S0036023622050187

45. P. Barmann, L. Haneke, J. M. Wrogemann, et al., ACS Appl. Mater. Interfaces **13**, 26074 (2021). https://doi.org/10.1021/acsami.1c05889

46. A. Dash, R. Vaßen, O. Guillon, et al., Nat. Mater. **18**, 465 (2019). https://doi.org/10.1038/s41563-019-0328-1

47. Q. Sun, J. Wang, X. Wang, et al., Nanoscale **12**, 16987 (2020). https://doi.org/10.1039/C9NR08350B

48. K. Zhu, Y. Jin, F. Du, et al., J. Energy Chem. **31**, 11 (2019). https://doi.org/10.1016/j.jechem.2018.03.010

49. R. B. Rakhi, B. Ahmed, M. N. Hedhili, et al., Chem. Mater. **27**, 5314 (2015). https://doi.org/10.1021/acs.chemmater.5b01623

50. J. X. Li, Y. L. Du, and C. Cui, Mater. Sci. Forum **833**, 44 (2015). www.scientific.net/MSF.833.44.

51. Y. Wang, W. Zheng, P. Zhang, et al., J. Mater. Sci. **54**, 11991 (2019). https://doi.org/10.1007/s10853-019-03756-6

52. S. Yazdanparast, S. Soltanmohammad, A. Fash-White, et al., ACS Appl. Mater. Interfaces **12**, 20129 (2020). https://doi.org/10.1021/acsami.0c03181

53. M. Wu, Y. He, L. Wang, et al., J. Adv. Ceram. **9**, 749 (2020). https://doi.org/10.1007/s40145-020-0411-8

54. M. Wu, Y. An, R. Yang, et al., ACS Appl. Nano Mater. **4**, 6257 (2021). https://doi.org/10.1021/acsanm.1c01059

55. H. He, Q. Xia, B. Wang, et al., Chinese Chem. Lett. **31**, 984 (2020). https://doi.org/10.1016/j.cclet.2019.08.025

56. M. Wu, B. Wang, Q. Hu, et al., Materials (Basel) **11**, 2112 (2018). https://doi.org/10.3390/ma11112112

57. B. Wang, A. Zhou, F. Liu, et al., J. Adv. Ceram. **7**, 237 (2018). https://doi.org/10.1007/s40145-018-0275-3

58. L. Zhang, D. Huang, P. Zhao, et al., Sep. Purif. Technol. **288**, 120718 (2022). https://doi.org/10.1016/j.seppur.2022.120718

59. X. Song, H. Wang, S. Jin, et al., Nano Res. **13**, 1659 (2020). https://doi.org/10.1007/s12274-020-2789-6

60. K. Maleski, C. E. Shuck, A. T. Fafarman, et al., Adv. Opt. Mater. **9**, 2001563 (2021). https://doi.org/10.1002/adom.202001563

61. A. S. Mokrushin, I. A. Nagornov, T. L. Simonenko, et al., Appl. Surf. Sci. **589**, 152974 (2022). https://doi.org/10.1016/j.apsusc.2022.152974

62. I. A. Nagornov, A. S. Mokrushin, E. P. Simonenko, et al., Russ. J. Inorg. Chem. **67**, 539 (2022). https://doi.org/10.1134/S0036023622040143

63. A. S. Mokrushin, T. L. Simonenko, N. P. Simonenko, et al., Appl. Surf. Sci. **578**, 151984 (2022). https://doi.org/10.1016/j.apsusc.2021.151984

64. E. P. Simonenko, A. S. Mokrushin, N. P. Simonenko, et al., Thin Solid Films **670**, 46 (2019). https://doi.org/10.1016/j.tsf.2018.12.004

65. T. L. Simonenko, N. P. Simonenko, P. Y. Gorobtsov, et al., J. Alloys Compd. **832**, 154957 (2020). https://doi.org/10.1016/j.jallcom.2020.154957

66. N. Xue, X. Li, L. Han, et al., J. Mater. Chem. A **10**, 7960 (2022). https://doi.org/10.1039/D1TA09981G

67. J. Xu, J. Shim, J.-H. Park, et al., Adv. Funct. Mater. **26**, 5328 (2016). https://doi.org/10.1002/adfm.201600771

68. M. Khazaei, M. Arai, T. Sasaki, et al., Phys. Rev. **92**, 075411. https://doi.org/10.1103/PhysRevB.92.075411

69. S. Hajian, S. M. Tabatabaei, B. B. Narakathu, et al., *Proceedings of the 2021 IEEE International Conference on Flexible and Printable Sensors and Systems (FLEPS), p. 1–4.* https://doi.org/10.1109/FLEPS51544.2021.9469784

Translated by V. Avdeeva